Delft University of Technology

Shape morphing of additively manufactured metallic kinematic structures to trace single- and doubly-curved surfaces

de Jong, Pier H.; Moosabeiki, Vahid; Leeflang, Marius A.; Mirzaali, Mohammad J.; Zadpoor, Amir A.

Important note
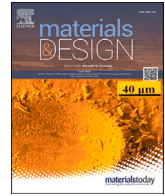To cite this publication, please use the final published version (if applicable).
Please check the document version above.

Shape morphing of additively manufactured metallic kinematic structures to trace single- and doubly-curved surfaces

Pier H. de Jong [ID],*, Vahid Moosabeiki, Marius A. Leeflang [ID], Mohammad J. Mirzaali [ID],*, Amir A. Zadpoor [ID]

Department of Biomechanical Engineering, Faculty of Mechanical Engineering, Delft University of Technology (TU Delft), Mekelweg 2, 2628 CD, Delft, the Netherlands

ARTICLE INFO

ABSTRACT

Biocompatible and shape-morphing metallic structures have been proposed for musculoskeletal applications to provide structural support to bony tissues. However, fabricating these structures to conform to a wide range of curvatures, including both single and double curvatures, remains a significant challenge. In this study, we present and analyze structures featuring a regular tiling network connected by spherical joints, forming a chain mail-like mechanism capable of adapting to complex geometries with clay-like flexibility. Simulations using a multibody kinematics model show that parameters such as unit cell shape, dimension ratios, and substrate curvature affect the shape-matching abilities of the structure. Experimental validation using specimens additively manufactured through laser-based powder bed fusion (from Ti6Al4V) and full-field strain measurements performed through digital image correlation confirms the simulation results, demonstrating that reducing structural density (*i.e.*, fewer bodies, struts, and joints per unit area) improves shape adaptability. However, the improved shape morphing capability often comes at the expense of mechanical strength under uni-axial tensile loads. These findings provide a framework for optimizing structures designed to achieve efficient surface conformance and adaptability in load-bearing applications.

1. Introduction

Medical devices perform better when closely conforming to each patient's unique anatomy. An anatomically tailored fit improves functionality and patient outcomes in applications requiring precise structural integration and stability. Examples of those are orthopedic implants and casts (Fig. 1a), or cloaking of the warping heart where the timing of each contraction demands precision by a stable fit [1]. However, achieving this level of customization presents a significant challenge. Therefore, a key question is whether medical devices should be individually tailored to each patient or if adaptable designs can be developed to fit a wide range of anatomies. Currently, there are two main approaches to addressing this issue: first, fully patient-specific devices, which provide a precise anatomical fit but are costly and time-consuming to produce, and second, generic devices, which are more scalable and affordable but lack precise customization. One of the primary geometric challenges of both approaches is accommodating complex curvatures (*i.e.*, single or double curvatures) that vary significantly between different anatomical regions.

This need for adaptable, shape-matching structures extends beyond healthcare [2]. It is also critical in fields such as robotics [3,4], aerospace [5], and automotive engineering [6,7], where components often need to interface with curved or irregular surfaces. In healthcare, particularly in musculoskeletal applications, advances in additive manufacturing and image-based design techniques have enabled the development of "patient-specific" devices that precisely match individual anatomies [8–19]. Clinical studies have shown that these customized devices reduce the stresses on surrounding tissues, promote faster healing, and improve integration with bone structures, resulting in better patient outcomes [17,20]. However, despite these benefits, patient-specific devices' high costs and extended production times limit their accessibility. While more affordable in manufacturing, mass-produced generic devices often require additional surgical adjustments [21] and can lead to longer recovery times and less favorable results [9,22].

The trade-off between customization and cost-effectiveness highlights a critical limitation of patient-specific devices [23,24]. While these customized devices offer improved clinical outcomes in treating

---

* Corresponding authors.
E-mail addresses: P.H.deJong@tudelft.nl (P.H. de Jong), M.J.Mirzaali@tudelft.nl (M.J. Mirzaali).

various musculoskeletal diseases [25], they are usually much more expensive than their generic counterparts. Most of the costs of patient-specific medical devices stem from the time-consuming and labor-intensive design process required to tailor each device to the anatomy of individual patients. As a result, it is often not feasible to use such medical devices to treat all patients who might benefit from such a customization process. Moreover, the long lead time required for the design of patient-specific implants (*e.g.*, up to six weeks for some orthopedic implants) makes them unsuitable for urgent surgical cases, such as trauma interventions. Although advanced planning techniques and additive manufacturing in the surgical process have helped reduce surgical times and costs [14,23,26–30], these approaches still require an intermediate step between diagnosis and treatment, limiting their practicality in time-sensitive situations.

To address these challenges, we proposed the concept of "metallic clay" [31], a design approach in which medical devices, in general, and orthopedic implants, in particular, are engineered to exhibit both shape-morphing and shape-locking capabilities. This concept enables the devices to adapt to various anatomical shapes during installation and maintain the required form once placed. Such shape-morphing behavior introduces the potential for "collectivized" implants, standardized medical devices that can still adapt to diverse anatomies. We could have a single implant design taken off the shelf and applied to various medical cases at hand. Thereby, it could extend the benefits of anatomy-matching to a broader patient population while reducing lead times and enabling their use in urgent interventions. The concept of metallic clay, however, is still in its infancy. While we have previously proposed a framework for the design of shape-morphing orthopedic implants [32], it has not yet been applied to complex geometrical challenges commonly encountered in actual surgical scenarios.

We define the principles of shape-morphing and possible locking of a structure as, respectively, the ability of the structure to take a specific shape and to maintain that shape due to constraints that remove degrees of freedom once a specific shape is achieved [31]. The morphing and locking can be activated through different methods [33]. In studying how well different designs can adapt to various curvatures, the kinematics of shape-morphing behavior is more important than the exact shape-morphing mechanism. As for the locking mechanism, we use an irreversible method appropriate for orthopedic implants [34,35]. Here, we investigate a pattern-to-pattern shape morphing [36] where the structure is shaped over a substrate through external influences, resulting in a "molded" structure. The locking process occurs by applying an external cement that irreversibly secures the structure over time.

Our previous studies explored the broad concept of "metallic clay" [31,32] and here we will investigate the characteristics of one implementation of the concept, namely a lattice structure that is inspired by chain mail (Fig. 1a–b). Traditional chain mail structures [37] are defined as a 2-D sheet but can change shape to become 3-D. The structure's nature also dictates a regular pattern in the connected moving parts. This network can be altered nonetheless, both in terms of pattern and in geometry. Hence, they are relatively simple structures that allow for experimenting with the effects of a comprehensible set of different parameters. Moreover, these structures combine the flexibility of shape adaptation with the structural strength required for load-bearing. This combination is particularly valuable for applications that require support around curved or irregular objects, such as covering cavities on curved surfaces or immobilizing joints on the human body. In the search for "metallic clay" lattice structures, we explored chain mail-like structures as a promising design principle, merging adaptability with mechanical strength. In particular, it is not yet clear how well various designs of shape-morphing implants can conform to complex curved surfaces, which are common in orthopedic applications. Here, we study how different designs of shape-morphing 3-D printed metallic structures adapt to complex geometries, focusing on the specific cases of curved surfaces. Curvature is one of the most important geometrical features in 3-D shapes [38–40]. Therefore, we explored how various design pa-

rameters, such as the configuration of the network connections and the length of structural struts, influence the ability of metallic lattices to conform to single- and doubly-curved surfaces.

The principles of traditional chain mail are replicated, but its design is adapted to gain new multibody structures. As also shown in another study [35], ball-and-socket joints replace loosely attached chain links to connect the rigid parts. This replacement allowed for better control over the deformation of the structure and increased strength. The small hinges between rigid components supplied the numerous degrees of freedom (DoF) required for the structures to achieve the necessary flexibility for conforming to diverse shapes. On this scale, powder bed fusion is an ideal, if not the only, manufacturing technique capable of creating such complex structures in a single, non-assembled process. However, designing these mechanisms to be fully printable presents significant challenges, requiring careful consideration of the limitations of current 3-D printing technology.

Both simulations and experiments were conducted to evaluate how various design parameters influence the performance of the structures. To this end, the structures were parametrized (Fig. 1b). Target shapes were varied according to one shape parameter (Fig. 1c). The simulations focused on modeling the kinematic behavior of the system, while the experiments assessed both the shape-matching capabilities and the mechanical properties of the 3-D printed structures. The shape-matching performance of the structures was assessed by measuring how well the structures conformed to the contours of curved surfaces, with deviations quantified to assess the accuracy. In addition to shape adaptability, we also investigated the load-bearing capacity of the additively manufactured metallic structures to ensure mechanical reliability.

For mechanical testing, digital image correlation (DIC) was used to capture the full-field strain data during uni-axial tensile tests conducted using custom-designed fixtures. The results from simulations and experiments were analyzed qualitatively and quantitatively to evaluate the kinematic and load-bearing performance of the proposed designs. Through this study, we aim to demonstrate the potential of shape-morphing metallic structures as adaptable, load-bearing medical devices capable of conforming to complex anatomical shapes, offering a promising alternative to fully customized implants.

2. Materials and methods

2.1. Structure lay-out

A sheet-like structure can be used to achieve surface conformity through kinematic deformation. The different components of this structure were arranged in a tiling, or tessellation fashion, to create a regular pattern and reduce the number of variables involved in the design process. Moreover, in this study, we restricted our focus on the periodic tilings with a rotational symmetry, based on regular polygons [41–43], to simplify the design of bodies connected through linkages and spherical joints. This periodicity enabled us with three possible body shapes constrained by crystallographic restriction, including equilateral triangles with three planes of symmetry, squares with four planes of symmetry, and hexagons with six planes of symmetry.

Two parameters fully defined each shape: the body "radius" r and the link length l (Fig. 1b). The total length $h = 2r + l$ was kept constant at $11.5\,\text{mm}$ across all experiments. Also, all shapes were arranged on a grid that fits within a square, with the distance from the center to the corner set at $75/\sqrt{2}\,\text{mm}$.

2.2. Definitions of shapes and curvatures

The shapes to which the structures conform were selected to reflect different signs of Gaussian curvatures. To come to a variety of curvatures in the selected surfaces for experimenting, we turned to surfaces of revolution [44]. The following parametric equations described these surfaces:
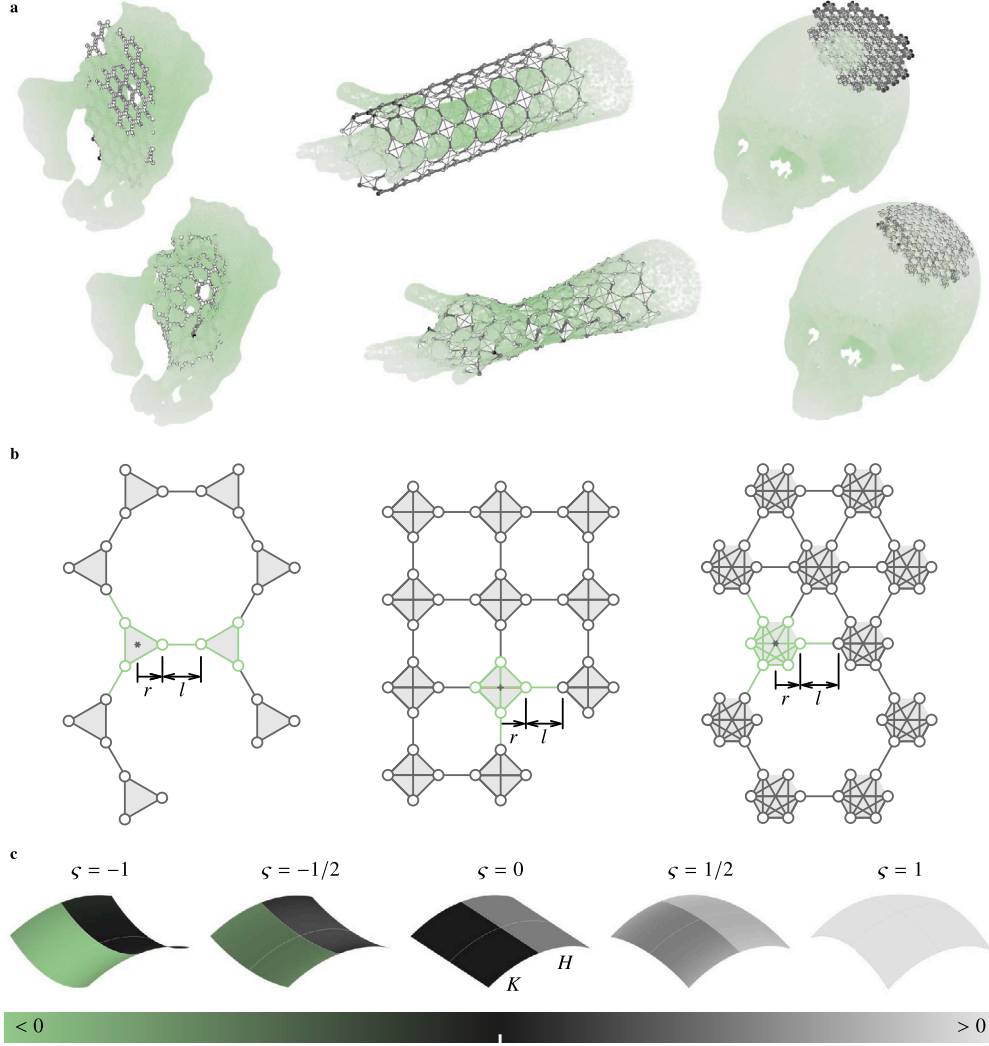
Fig. 1. Illustrations of the considered lattice structures and the shapes they conform to. **a** Three possible applications where a lattice structure takes the shape of objects with a variety of curvatures; an acetabulum, lower arm, and skull. **b** Three in-plane layouts of the lattice maille-like regular tiling structures: triangles (trigons), squares (tetragons), and hexagons. The body shape of the lattice structure was fully defined by a "radius" r and a link length l, modeled as a system of nodes (circles) and constraints (lines). **c** The surfaces were created from the "toroidal" expression $(x, y, z) = (\rho \cos v, a \sin u, \rho \sin v)$, with $\rho = a(\varsigma \cos u - \varsigma + 1)$, where $-\pi/2 < u < \pi/2$, a is the length of one semi-axis ($\{a\} = 1$ in figure examples), and ς is a factor that relates the second semi-axis to the first.

$$(x, y, z) = (\rho(u)\cos v, \, y(u), \, \rho(u)\sin v), \tag{1}$$

where ρ is the varying radius along y. Different equations for ρ and y give different sets of surfaces as depicted in Table 1 and Fig. 2.

The definite set of surfaces for experimenting includes curvatures of all signs and allows one to change curvature by adjusting one parameter. This set is shown in Fig. 1c. It has

$$\rho = a(\varsigma \cos u - \varsigma + 1), \qquad y = a \sin u, \tag{2}$$

where $-\pi/2 < u < \pi/2$, a is the length of one semi-axis, and ς is a factor that relates the second semi-axis to the first (Fig. 1c). The Gaussian K and mean curvature H of these surfaces are given by:

$$K = \frac{\varsigma \cos u}{a^2(\varsigma^2 - \varsigma^2 \cos^2 u + \cos^2 u)^2 (\varsigma \cos u - \varsigma + 1)}, \tag{3}$$

$$H = \frac{\varsigma + 2\varsigma^2 \cos u + \cos^3 u - \varsigma^2 \cos^3 u - \varsigma^2}{2a \, |\varsigma \cos u - \varsigma + 1| \left(\varsigma^2 + \cos^2 u - \varsigma^2 \cos^2 u\right)^{3/2}}. \tag{4}$$

Note that this sign from the mean curvature comes from the (arbitrary) definition of the surface normal that is positive when pointing "away from" the axis of revolution. For certain values of ς when $-\pi/2 < u < \pi/2$, we obtain

$$\varsigma = -1 \quad \Rightarrow \quad K = \frac{\cos u}{a^2(\cos u - 2)}, \qquad H = -\frac{\cos u - 1}{a(\cos u - 2)}, \tag{5}$$

$$\varsigma = 0 \quad \Rightarrow \quad K = 0, \qquad H = \frac{1}{2a}, \tag{6}$$

$$\varsigma = 1 \quad \Rightarrow \quad K = \frac{1}{a^2}, \qquad H = \frac{1}{a}. \tag{7}$$

For our experiments, we set $a = 10(\frac{1}{2} + \frac{1}{2}\sqrt{5})^{-1}h$.

2.3. Experimental morphing, locking, and testing

The morphing and locking process was conducted by combining the structures with shape substrates. After manufacturing, the structures were morphed into the target shapes to verify their shape-morphing capabilities as predicted by the simulations. Once the structures were morphed into the desired shapes, they were locked in place to enable further analysis.

These structures were manufactured through laser-based powder bed fusion of medical-grade Ti6Al4V ELI (PBF-LB/ M/ Ti6Al4V. SLM125, ReaLizer GmbH, Germany, Table 2). Design principles followed those required for non-assembly AM with this technique [31,48], taking into account tolerances and overhang angles. For example, the structures were
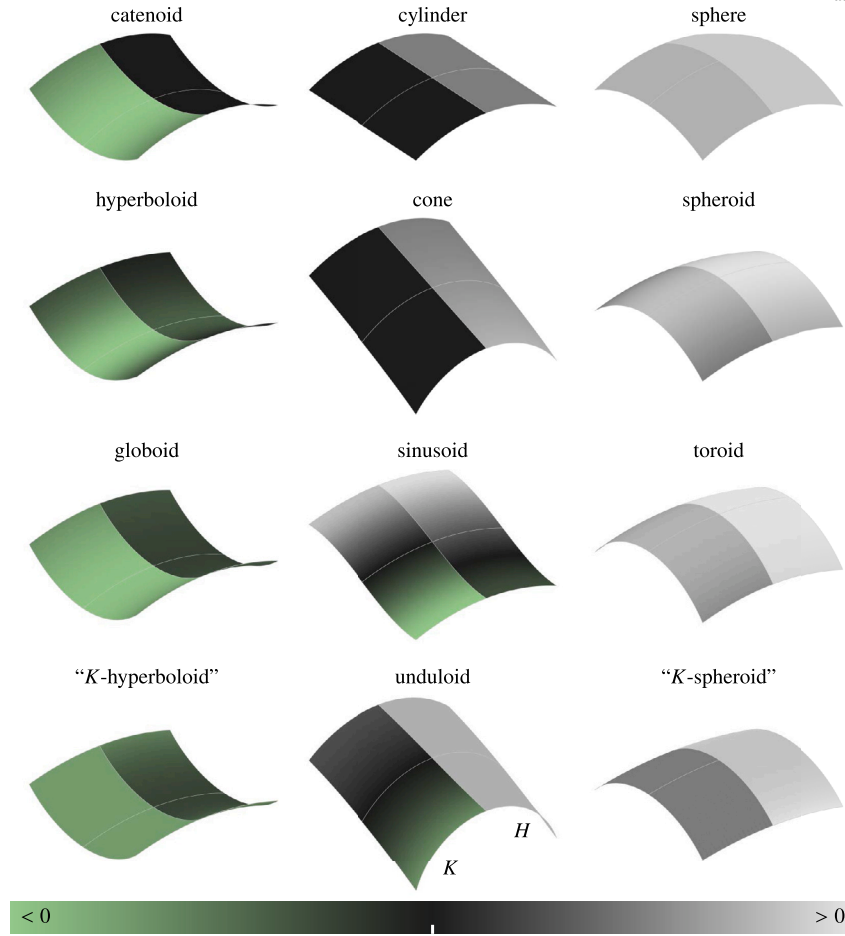
Fig. 2. Different extracts of surfaces of revolution with Gaussian curvature K and mean curvature H. One can see how the curvature develops over the length of the surface, with on one half (left) the colors associated with Gaussian curvature and on the other half (right) the mean curvature. Constant curvatures over the surface are identified by constant colors; no gradient. Note that the direction of the surface normal is defined positive when pointing "away from" the axis of revolution, such that the color shading is the most convenient to interpret.

Table 1

Different surfaces of revolution with their radius and longitudinal coordinates. The full set of 3-D coordinates is obtained by revolving a curve around the y-axis with $(x, y, z) = (\rho(u)\cos(v), y(u), \rho(u)\sin(v))$. Some equations require conditions on the parameters to ensure the shape has a correctly associated name. Note that the non-listed plane is the only surface with $K = 0$ and $H = 0$.

|	radius	longitude	notes
cylinder	$\rho = a$	$y = u$	$K = 0$, $H = $ constant
cone	$\rho = au$	$y = u$	$K = 0$
sinusoid	$\rho = a\cos(u\pi) + b$	$y = u$	$b \geq a$
catenoid	$\rho = a\cosh(u/a)$	$y = u$	$H = 0$
globoid	$\rho = -a\cos(u) + b$	$y = a\sin(u)$	$-\frac{\pi}{2} \geq u \geq \frac{\pi}{2}$, $b \geq a$, [44]
toroid	$\rho = a\cos(u) + b$	$y = a\sin(u)$	$-\frac{\pi}{2} \geq u \geq \frac{\pi}{2}$, $b \geq a$
sphere	$\rho = a\cos(u)$	$y = a\sin(u)$	
spheroid	$\rho = a\cos(u)$	$y = b\sin(u)$	
hyperboloid	$\rho = a\cosh(u)$	$y = b\sinh(u)$	
"K-spheroid"	$\rho = ab\cos(u)$	$y = a\int_0^u \sqrt{1 - b^2\sin^2(\varepsilon)}\,d\varepsilon$	$b > 1$, $K = $ constant, [45,46]
"K-hyperboloid"	$\rho = ab\cosh(u)$	$y = a\int_0^u \sqrt{1 - b^2\sinh^2(\varepsilon)}\,d\varepsilon$	$K = $ constant, [45,46]
unduloid	$\rho = \sqrt{\frac{b^2-a^2}{2}\sin\left(\frac{2u}{a+b}\right) + \frac{b^2+a^2}{2}}$	$y = a\int_0^{\frac{u}{a+b} - \frac{\pi}{4}} \sqrt{\left(1 - \frac{b^2-a^2}{b^2}\sin^2(\varepsilon)\right)^{-1}}\,d\varepsilon$ $+ b\int_0^{\frac{u}{a+b} - \frac{\pi}{4}} \sqrt{1 - \frac{b^2-a^2}{b^2}\sin^2(\varepsilon)}\,d\varepsilon$	$b \geq a$, $H = $ constant, [47]

Table 2

Manufacturing process parameters used for the laser-based powder bed fusion.

	contour	hatch
slice height	50 μm	50 μm
laser power	88 W	88 W
exposure time	20 μs	5 μs
point distance	10 μm	10 μm
scanning strategy	–	90° alternating
hatch distance	–	150 μm
hatch offset	–	80 μm

designed so that individual kinematic components were self-supporting, allowing joint clearance to be created without the need for support structures, making the structures functional immediately after removal from the build plate. The alloy, with an elastic modulus of about 110 GPa, ensured that in unlocked state the deformation is purely kinematic. Moreover, the material was medical grade, demonstrating the potential for future medical applications.

This method included custom molding and mechanical testing fixation. Substrate shapes were fabricated beforehand from silicone cast rubber (Poly-Sil PS 8520, Poly-Service, The Netherlands). The negative of the desired shape was printed with polylactic acid (PLA) using material extrusion (MEX-TRB/P). This negative was then used to pour the silicone rubber on, and in an overpressure, it was left to dry for
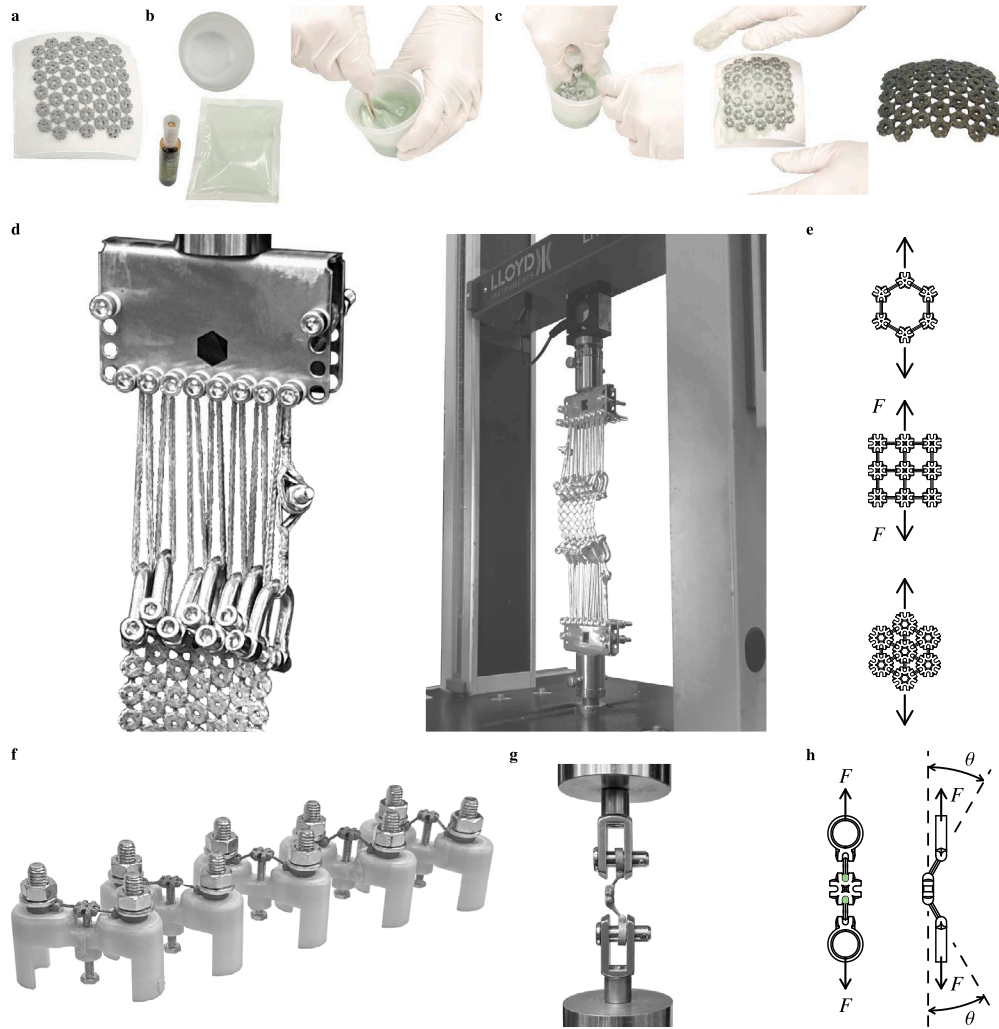
Fig. 3. Molding, fixation, and mechanical testing of the samples. **a** A silicone rubber substrate shape (sphere in this example) with a structure laying on top of it. **b** The molding process with mixing the components, **c** submerging the structure in the cement, and molding it manually on the substrate (a sphere in this example). **d** The samples in the test setup. A detail of the custom fixture for a structure sample (saddle in this example) suspended in the testing machine and an overview of the testing rig with a structure and a DIC setup illuminating it. **e** A schematic drawing of the loading directions for the different body shapes, showing applied (resultant) force F. **f** The holders for setting individual bodies with different link angles during molding. Cement was applied to the angled joints through a syringe. **g** A sample mounted in the test setup. **h** A schematic drawing of the setup, showing the applied force F and set angle θ. Green dots indicate the locked spherical joints.

a day. The result was a rubber substrate representing a desired shape on which the structures could be positioned (Fig. 3a). A low-viscosity two-component bone cement (PALACOS® LV, Heraeus Medical GmbH, Germany) was prepared according to the manufacturer's instructions (Fig. 3b). Within two minutes of preparation, the structure was submerged in the cement and was crumpled twice (Fig. 3c). Subsequently, redundant cement was percolated out, and the structure was folded and smoothed on the substrate. Finally, the cement was allowed to cure under an overpressure of 2 bar for ten minutes, after which the structures were removed from the substrate. The whole molding process is demonstrated in Supplementary Video 1.

A custom fixture was designed to suspend the samples in the mechanical testing bench (Fig. 3d). The main idea behind this testing was to investigate the degree to which the samples were locked, *i.e.*, to investigate their deformation resistance after the cement was applied. For comparison purposes, the testing method should apply similar loading conditions to all structures in all shapes to look at shape effects solely. Therefore, we chose to take the morphed and locked structures and apply loads that attempt to pull them back into their neutral, straightened configuration. The shape-morphing structures underwent uni-axial ten-

sile testing until failure, where the fixture ensured that forces remained in the plane at each point, minimizing any additional bending on the structure. The applied force is distributed equally over the bodies on an edge. Harp closures were modified to tighten them on individual bodies by screwing. On either side of the sample, one wire (Dyneema, Avient Corporation, USA) is laced between these harps and a "block" at the testing rig side in a zigzag manner. The structures were oriented under the load F as depicted in Fig. 3e.

Separate body elements were also manufactured to test the effects of link angles θ on the strength under a load F (Fig. 3e–g). The separate body elements were subjected to uni-axial tensile tests at different linkage angles θ, while the spherical joints were fixed using bone cement. The molding of the individual bodies was done by first setting the angles of the links in custom-made holders that allowed setting the angle by adjusting a screw (Fig. 3f). The cement was then prepared, as previously mentioned, but this time was applied through a syringe. The individual bodies with different angles had rings (with unlocked spherical joints) that could be fixated as shown in Fig. 3g and pulled straight. The uni-axial load F and link angle θ are oriented as shown in Fig. 3h.
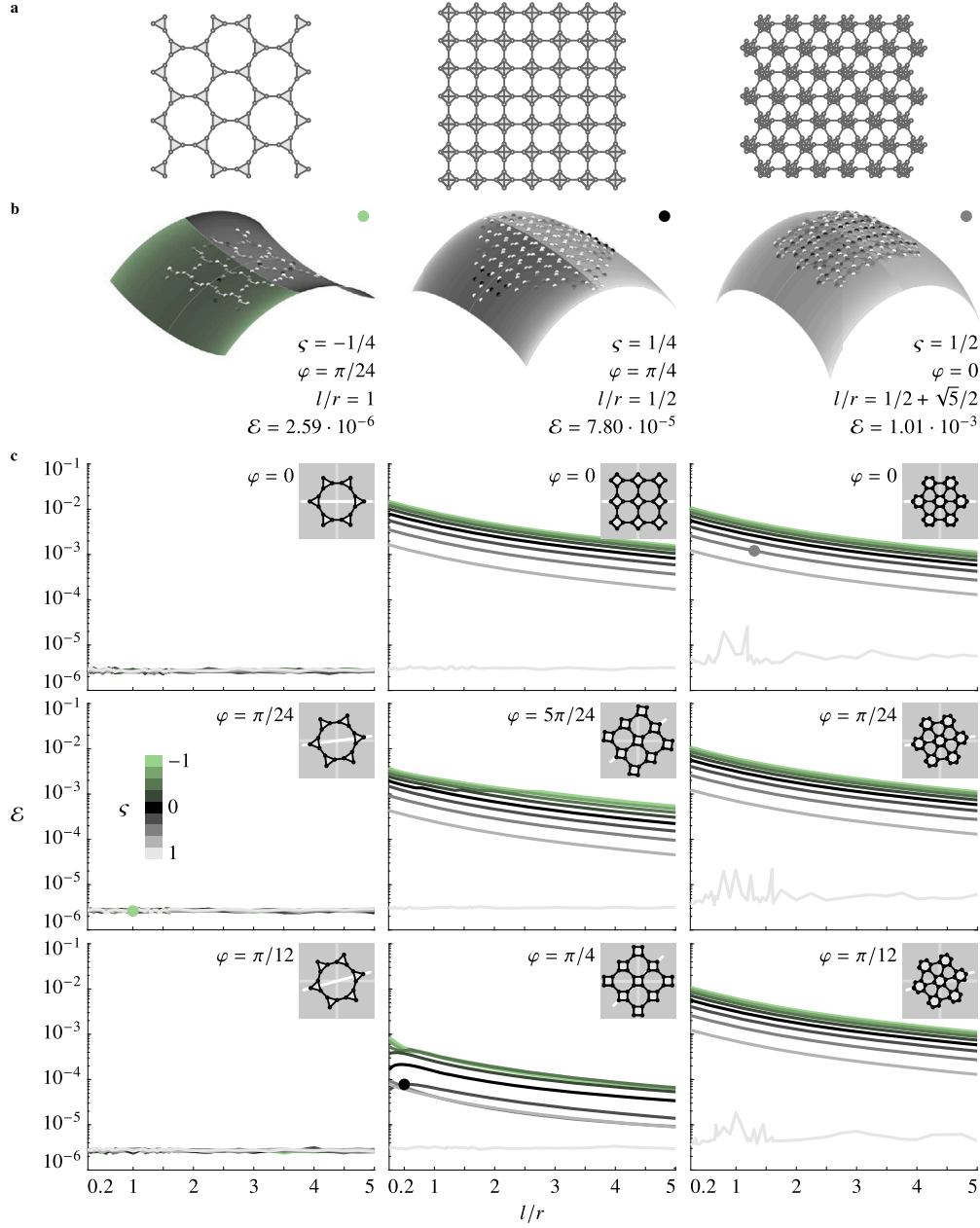
Fig. 4. Shape-morphing simulations of the three structures into different surfaces of revolution. **a** The different structures were lattices with a specific number of bodies and l/r (link length over body radius) ratio per body shape. **b** Three examples of shape-morphing simulations for surfaces with a semi-axis radius $a = 10(\frac{1}{2} + \frac{1}{2}\sqrt{5})^{-1}h$, with $h = 11.5$ mm. The shape variable ς determined whether the surface was a saddle, cylinder, or ellipsoid (*i.e.*, has negative, zero, or positive Gaussian curvature). Rotation angle φ described the orientation of the structure with respect to the surface about a radial axis. The cumulative error $\mathcal{E}$ quantified how well the structure conformed to the surface. The shading of individual nodes depicts the local error at the node location, with a darker shading indicating a larger error. **c** Graphs showing cumulative error values $\mathcal{E}$ for all simulations, varying ς, l/r, and φ. Note that the curvature shade values were normalized as $\hat{K} = a^2 K$ and $\hat{H} = aH$ for more contrast.

2.4. Simulation of the morphing process

To predict the shape-morphing qualities of the structures with respect to these shapes, we used a kinematic multibody approach developed in our previous study [32]. The structures were modeled as systems of nodes and constraints. The nodes defined the corners of the bodies and represented the center of spherical joints, while distance constraints (*i.e.*, links) connected the nodes of adjacent bodies. The different structures were lattices with 28 triangular, 49 square, and 45 hexagonal bodies (Fig. 4a). All simulated lattices had $h = 2r + l = 11.5$ mm with varying link length over body radius ratio l/r.

The morphing algorithm adjusts the positions of all nodes $\boldsymbol{x}$ to make the structure conform as closely as possible to a target shape. All possible linear motions $\mathbf{U}$, subject to constraints, were computed by solving $\mathbf{JU} = \mathbf{0}$, where $\mathbf{J}$ is the Jacobian of the constraint vector. Subsequently, the nodes were moved toward their target positions on the surface $\boldsymbol{x}_\mathrm{g}$ to obtain a new set of coordinates as $\boldsymbol{x}_* = \boldsymbol{x} + \mathbf{U}((\mathbf{U}^\mathrm{T}\mathbf{U})^{-1}\mathbf{U}^\mathrm{T}(\boldsymbol{x}_\mathrm{g} - \boldsymbol{x}))$. Due to the linear nature of the motions, this process requires several iterative steps. Note that the target positions $\boldsymbol{x}_\mathrm{g}$ were determined by minimizing the Euclidean distance between the current node positions and the parametric surface described by (1). The residual distance error is

$$\mathcal{E} = h^{-1} \sqrt{n^{-1}(\boldsymbol{x_g} - \boldsymbol{x}) \cdot (\boldsymbol{x_g} - \boldsymbol{x})}, \tag{8}$$

with the total number of nodes n, and the constant characteristic length $h = 2r + l$. This error serves as a metric for how well the structure is able to replicate the shape, with a smaller error indicating a better fit. When the distance error stopped to decrease between iterations (with a tolerance of $1 \cdot 10^{-6}$), the minimum was reached.

We varied three parameters, including body shape, the ratio of link length to body radius l/r, and the rotational placement angle φ about the vertical axis relative to the substrate (Fig. 4). Structures with different body shapes were initially created in a flat configuration that fits within the defined total grid radius with $h = 11.5$ mm (Fig. 4a). The ratio l/r was varied from 0.2 to 5 for all three body shapes, as illustrated in Fig. 4b. For the rotational angle φ, we chose three different orientations, including i) alignment with a symmetry plane of the substrate, ii) no alignment with any substrate plane, and iii) alignment with a plane rotated by $\pi/4$ about the vertical axis with respect to a symmetry plane (Fig. 4b–c).

2.5. Structure and substrate selection

Three structures were designed to represent the simulated grids of nodes and links (Fig. 5a). For printing support, the spherical joints needed an open side. This also resulted in a wider range of motion for the joints on two sides. The different designs of the structures were lattices with 45 triangular, 49 square, and 45 hexagonal bodies (note that these numbers are different from the simulations because of structural integrity). All lattices had a thickness of 2.6 mm and $h = 2r + l = 11.5$ mm with varying l/r (link length over body radius) depending on the body shape. The l/r values were chosen based on physical design limitations. For instance, the sockets of the spherical joints must touch each other to form a complete body. Consequently, the triangular bodies have the smallest radius, followed by the squares and then hexagons. Nine different locked structures, corresponding to different shapes, were created and compared with the simulations. Furthermore, three different substrate shapes were created to morph the structures into specific distinct shapes: saddle, cylinder, and spheroid (Fig. 5b). Each combination of structure and shape was repeated three times, resulting in a total of 27 specimens.

The shapes of the morphed structures were captured by 3-D-scanning (Scan-in-a-Box-FX, Open Technologies S.r.l., Italy) (Fig. 5b). Subsequently, the point clouds resulting from these scans were fitted on the surfaces' parametric description (1). The fitting algorithm considered all points of the cloud of one scan and minimized the cumulative distance to the surface. Finally, with every point considered as a node, the error metric (8) accompanying this fit quantified how closely the structures conformed to the target shapes.

A better shape fit is expected to result in more uniform force distribution and smaller stress concentrations by distributing the force with a larger contact surface. Mechanical tests were performed to investigate how body and substrate shape affect the structures' strength. The mechanical testing included uni-axial tensile tests to assess the structures' resistance to returning back to their initial, flat configurations after being morphed to a desired shape. This analysis provided insight into the structure's joint strength and overall structural resilience. Individual body elements with five different link angles ranging from 0° to 60° were tested separately to get insight into the angle effect. These as well as all the shape-morphing structures were tested using a mechanical testing bench (LLOYD instrument LR5K, Hampshire, United Kingdom, 5000 N load cell) at a rate of 2 mm min^{-1} until failure. A specific specimen's weight normalizes the structures' reported load as $\hat{F} = (mg)^{-1} F$, with a specimen's mass m and $g = 9.81$ m s^{-2}.

In total, 27 locked shape-morphing specimens (three design groups times three shapes per three replicates) were experimentally tested. The mechanical testing machine recorded load and displacement data. We captured the true strain τ maps (the equivalent von Mises strains) at a frequency of 1 Hz using a 3-D digital image correlation (DIC) system (Q-400, two cameras 12 megapixel each, LIMESS GmbH, Krefeld, Germany) and its associated software (Instra 4D v4.6, Danted Dynamics A/S, Skovunde, Denmark). For this purpose, we painted all the specimens white, followed by the application of a black dot speckle pattern.

3. Results and discussion

### 3.1. Simulation results of the shape-morphing process

The shape-morphing simulation results showed how the design parameters influenced the quality of the shape fitting (Fig. 4b–c). Overall, the shape-fitting error decreased (*i.e.*, the fit improved) with a reduction in the number of body vertices for the tested l/r with $\mathcal{E}$ around the order of 10^{-2} to 10^{-3} for hexagons, around the order of 10^{-3} to 10^{-4} for squares, and around the order of 10^{-6} for triangles. A decrease of about one order of magnitude (10^{1}) can be seen for an increase in l/r in the selected range from 0.2 to 5. Moreover, the error decreased as we moved from saddle to cylinder to spheroid surfaces with also approximately one order of magnitude (10^{1}) for all structure types at specific l/r. For triangular body shapes, in particular, the error remained consistently small, and neither l/r nor the substrate shape significantly affected the fit (Fig. 4c). In contrast, the error decreased with l/r for square bodies, and the fit improved as we moved from saddle to cylinder to spheroid surfaces. Moreover, for the square bodies, the rotational orientation of the structure φ relative to the substrate influenced the error, with smaller errors occurring when linkages were less aligned with the symmetry planes of the substrate. Here, the error decreased from the 10^{-2} to 10^{-4} range to the 10^{-3} to 10^{-5} range. The error similarly decreased for hexagonal bodies with l/r and as we moved from saddle to cylinder to spheroid surfaces. However, unlike square bodies, the rotational orientation φ has negligible impact on the error for hexagons. By comparing all simulations per body shape (*i.e.*, adding the errors per body shape for all respective orientations), we can conclude that the triangular shapes consistently provided the best fit, followed by square and hexagonal bodies.

The observed effects of design parameters on the shape-matching error can be explained by considering the geometry of the bodies. Triangular bodies, with three vertices, behave like a three-legged stool. All three vertices can easily contact the substrate surface on surfaces with reasonably small curvature, regardless of the curvature's sign or orientation. Square bodies exhibited larger errors overall, and their orientation plays a key role in whether all four vertices can contact the surface. When square bodies were aligned with the principal curvature lines of the substrate, the error was largest, while increasing the angular diversion from these principal curvature lines reduced the error. Another significant factor for square bodies was the l/r. Larger l/r values led to better fits, as smaller bodies with more than three vertices positioned closer to the surface improved shape conformity. Similarly, the error was smaller for larger values of the Gaussian curvature. Hexagonal bodies showed similar trends to square bodies, though the effects of orientation were minimal. This is because the hexagonal shape, which approximates a circle, has more symmetry axes, reducing the influence of orientation.

3.2. Experimental results

The 3-D printed structures made from different unit cell designs were able to morph into various shapes with different curvature values (Fig. 5). The structure designs, including the maximum manufacturing area, were adjusted to meet the printer's constraints (Fig. 5a). On the shape-morphed structures, we performed a qualitative analysis based on the results of the 3-D-scans (Fig. 5b) and compared these results with those of the simulations (Fig. 5c). For all three body shapes and their
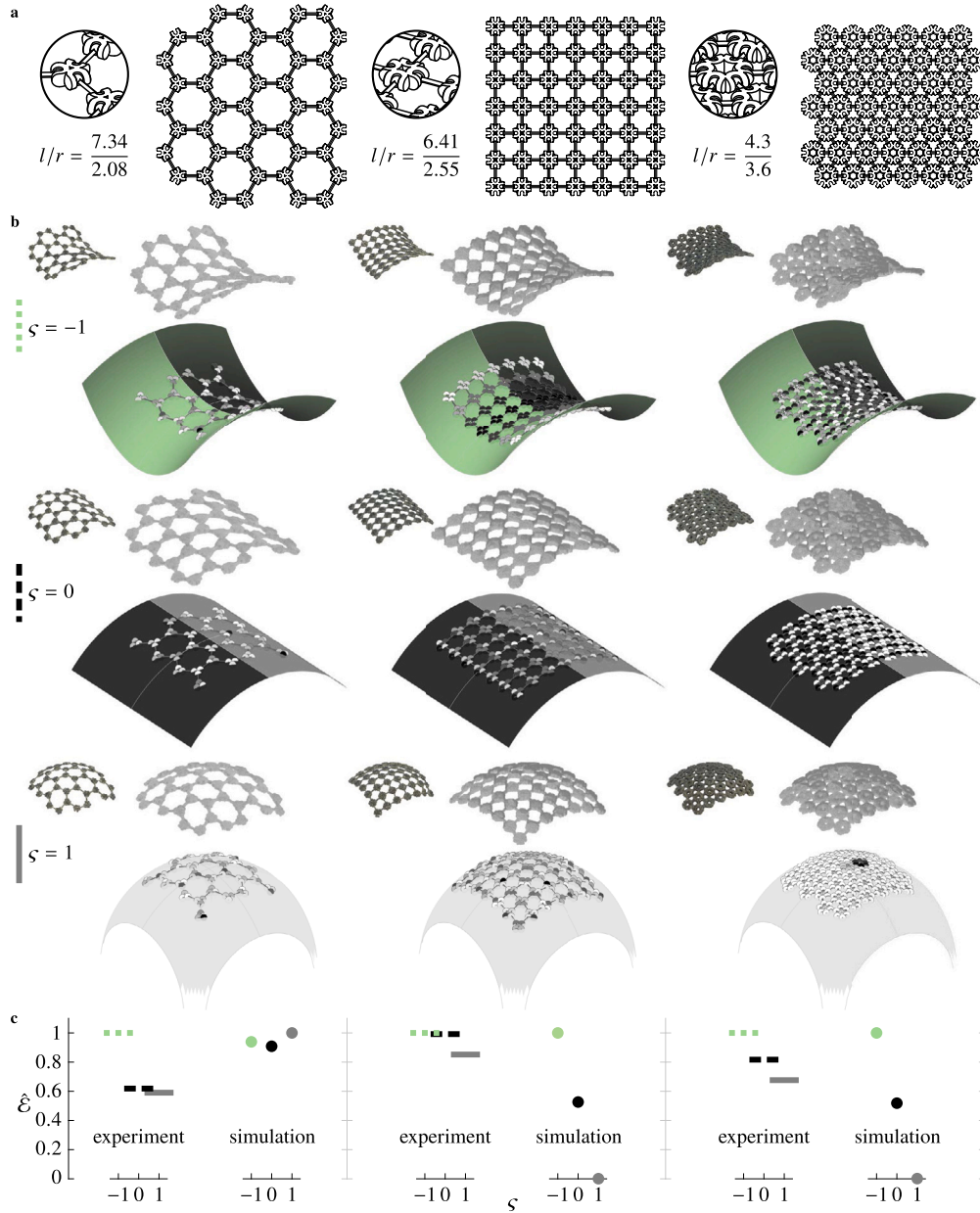
Fig. 5. Shape-morphing experiments of three structures onto three surfaces. **a** The different structures with a specific number of bodies and l/r (link length over body radius) per body shape. **b** Visual comparison of the experiments by photographed, 3-D-scanned, and simulated images. Structures were additively manufactured (PBF-LB) and shaped into molds representing the respective surfaces of revolution with $a = 10(\frac{1}{2} + \frac{1}{2}\sqrt{5})^{-1}h$, $h = 11.5\,\text{mm}$, and three ς values. Bone cement locked them into shape. 3-D-scans show how the experimental shapes compared to the simulated structures. **c** The 3-D-scans (experiments) were compared to the surfaces by calculating the normalized errors $\hat{\mathcal{E}}$. For each body shape, the errors were respectively normalized with respect to the largest error found in experiments and simulations. Note that the curvature shade values were normalized as $\hat{K} = a^2 K$ and $\hat{H} = aH$ for more contrast.

respective experimental and simulated values (six data sets), we normalized the per-set error with respect to the maximum error of each set. The earlier noted simulation trend, where the saddle shape shows the most error, followed by the cylinder and the sphere, is also noticeable in the experimental findings. However, for the same body shape, the differences between some substrate shapes are so minor in some instances that definite conclusions cannot be drawn. This part of the study, where shape morphing is quantitatively compared among experiments and simulation, is affected by the uncertainties that arose in the manual molding procedure. Note also that absolute values were not presented because these vary among the physical structures having finite thickness, and the model assumes zero thickness.

The experimental results partially validated the simulations. We confirmed that spherical shapes were easier to conform to than saddle shapes. The fitting errors for the cylindrical shapes were between those of the spherical and saddle ones. This might be a surprising result, since the spherical and saddle (hyperbolic) shapes are doubly curved or non-Euclidean, compared to the single curved or Euclidean cylinder shape [38,39]. A paper sheet cannot be bent into a doubly curved surface without being stretched in its plane. However, the structures presented here allow in-plane motions. The individual bodies in the structure can reorient with respect to each other under bending. Consequently, spherical shapes can be replicated better than cylindrical shapes. The differences between individual body shapes were not evident from the raw measurements before the normalization. However, qualitatively, triangular structures were easier to morph on different substrates, which was consistent with the results of simulations emphasizing that triangular bodies can provide the best fit compared to squares and hexagons.
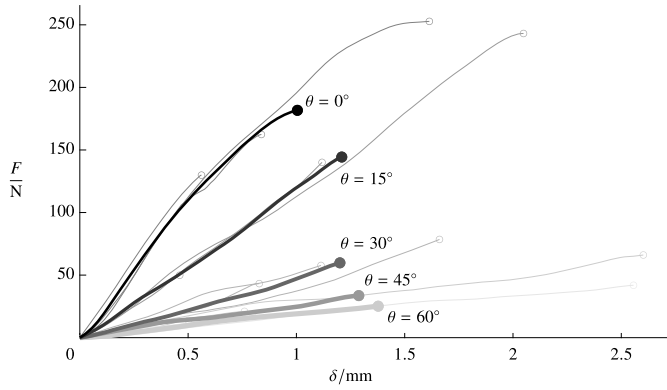
Fig. 6. Mechanical test results of individual bodies with struts fixated at different angles. A plot of the applied force F vs. the displacement in the force direction δ for different angles θ. Bold lines represent the average of three specimens for each angle (thin lines with open circles show individual specimens).

Table 3
Mechanical test loads at fracture F_f of individual bodies with struts fixated at different angles θ. The load is the average of three specimens for each angle.

θ/ °	F_f/N
0	181.7 ± 63.67
15	144.3 ± 96.67
30	59.80 ± 17.74
45	33.61 ± 28.33
60	25.15 ± 14.47

3.3. Load-bearing capabilities

The load-bearing performance of each individual linkage was assessed through mechanical tests at various angles of positioning (Fig. 6 and Table 3). The average maximum force at fracture showed that a larger linkage angle θ relative to the neutral position resulted in lower resistance to loads F. The increased linkage angle enlarges the moment arm of the applied force, and, thus, the same (bending) moment on the linkage and joint is reached with a lower F. Given that the locking was performed using bone cement, failures could theoretically occur either by a fracture in the struts of the lattice structure or by a detachment of the bone cement at the ball-and-socket joints. However, in our tests, all the specimens exhibited failure through a fracture in the struts, with no detachment at the joints.

The absolute strains before failure over the structures during mechanical loading show similarities as well as differences for the different structures and shapes (Fig. 7a). For all structures, the highest strains were found at the struts with values around 2%. The strains in the individual bodies in the structures differ among body and structure shapes. Triangular bodies overall experienced the least absolute strain $(0 - 1\%)$, followed by square $(0 - 1.5\%)$ and then hexagonal bodies $(0 - 2\%)$. The substrate shapes also influenced the strain distribution with analogies to thin plate theories. We found no clear distribution for the saddle, the cylinder has the least strain $(0 - 0.5\%)$ along the "peak ridge", the spheroid has the least stress concentrated around the "peak" of the dome $(0 - 0.5\%)$. The mechanical tests reveal that their geometry and the applied loading direction influence fracture and strain patterns in each structure. In the saddle configuration, fractures occurred along axes deviating 45 degrees from the loading direction, where the interaction of the concave and convex curvatures creates high bending stresses. In the cylindrical shapes, strain was concentrated along the central axis perpendicular to the load, while in spheroidal shapes, strain was localized at the edges, where stress concentrations formed due to curvature

Table 4
Mechanical test normalized loads at fracture for the different designs locked in the three different shapes. $\hat{F}_f = (mg)^{-1} F_f$, where F_f is the applied load at fracture, m is mass of the specific specimen, and $g = 9.81\,\mathrm{m\,s^{-2}}$.

$\hat{F}_f$/N	triangular	square	hexagonal
saddle	591.1 ± 204.1	845.4 ± 127.3	3086 ± 1558
cylinder	1537 ± 378.6	1986 ± 338.1	3834 ± 1907
sphere	920.3 ± 133.2	1345 ± 356.5	3192 ± 2581

uniformity disruption. Additionally, cylindrical structures exhibited the highest fracture load, followed by spheroids and then saddles (Fig. 7b). Fracture loads increased on average from triangular to square to hexagonal bodies respectively (Table 4). Note that there was no normalization with respect to the applied load, meaning that the larger raw strain values presented here might be caused by higher applied loads, rather than by structural behavior alone.

3.4. General discussion

In evaluating the performance of the structures, we observe a trade-off between shape-matching ability and locking strength. Structures with fewer vertices and smaller body sizes exhibited better shape conformity, but this comes at the cost of reduced locking strength when subjected to loads that attempt to return the structure to its original flat configuration. The triangular and hexagonal bodies represented two extremes: triangular bodies, with fewer interconnections, deformed more freely and were easier to crumple randomly, but also exhibited weaker resistance to deformation once locked.

With these insights on the principles of one-size-fits-all structures in hand, we can work more toward applications. One example is fixing defects in the human acetabular bone. A study on this led to the development of a novel implant [35]. The structure, featuring hexagonally shaped bodies, serves as the base for developing the implant, as it offers the highest mechanical strength while still exhibiting sufficient flexibility to conform to the most pronounced acetabular curvatures.

Another option for further research is the design and creation of specific sheet layouts. The structure is then specific to anatomical sites, but not to individual patients. It could be possible to introduce different body shapes in one sheet, to have some parts deform easier, while other parts are stronger. Methods like machine learning can aid in finding appropriate designs. In this light of versatility, sheets like the ones presented in this study are also of interest for fields like soft robotics. They can possibly be manufactured from different materials and with no or an alternative locking system. Design parameters of the structures could be optimized by simulation in such a way that the structure fits on the surface. Then, either different optimal structures for different surface curvatures are obtained, or one general structure can be designed that fits best on average on all possible curvatures. Optimized structures for different surface curvatures can be obtained to result in a one-fit-all structure that fits best on average on all possible curvatures and serves a wide variety of cases.

The mechanical properties were investigated from a geometric rather than a material perspective. We were only interested in the structural effects of the designs, and only a single production method for the structures was considered. This meant that the limits of the AM method dictated the envelope of possible structural designs. The ball-and-socket joints design allowed the balls to rotate freely within the sockets without requiring support during manufacturing. The struts had a diamond-shaped cross-section for the same reason: they did not require production support. These key elements of joints and struts were kept equal among all designs to ensure comparability. When changing joint and strut designs, the absolute load values that the structures can withstand change, but the trends observed between the structures with different layout designs and shapes remain relatively similar. Moreover, we used
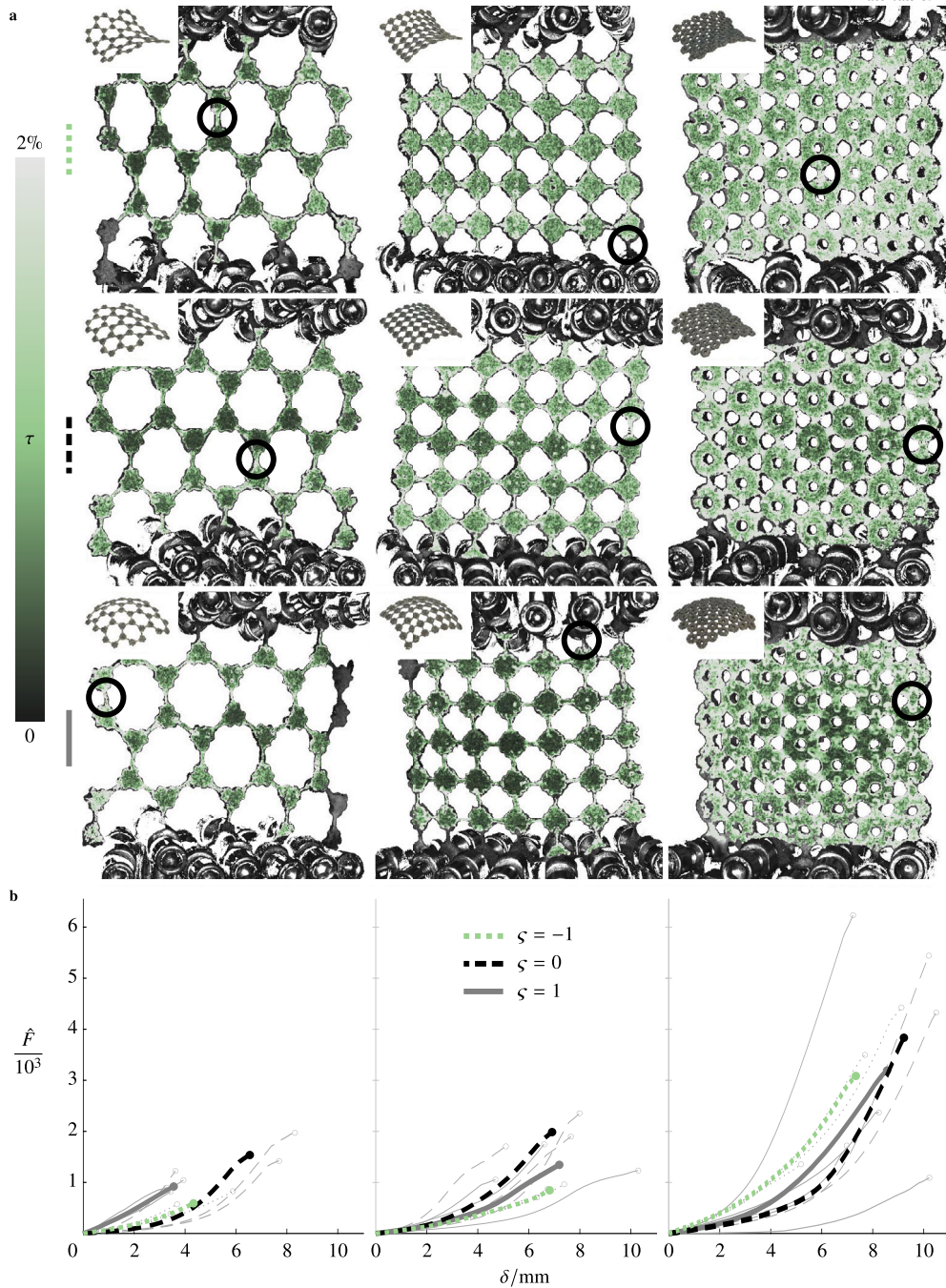
Fig. 7. Mechanical testing of the different designs locked in the three different shapes, namely saddle, cylinder, and sphere. **a** The structures were clamped at all bodies on two opposing edges to evenly distribute the applied force. The shading shows the true strain τ distribution obtained with digital image correlation (DIC) right before appearance of the first fracture as indicated by circles. **b** Applied load F *vs.* the average displacement δ for the different shapes defined by ς. The force is normalized with respect to the weight ($\hat{F} = (mg)^{-1}F$, with mass m and $g = 9.81\,\mathrm{m\,s^{-2}}$) of the specific specimen.

the same material to manufacture all the specimens. A different choice of material with similar stiffness and a similar layer-by-layer production method is expected to result in similar morphing behavior. Moreover, the relative performance of different designs in terms of the mechanical loads they can bear is expected to remain similar, regardless of the exact underlying material, as the structural design is the most dominant factor in determining the loading regime, stress concentrations, and even fracture sites. If the used material and manufacturing method produce more compliant parts, the shape-matching abilities may increase somewhat.

Shape morphing in this study is performed while the cement is already applied to the joints, which might thus affect the morphing. The viscosity of the cement is comparable to that of dish soap in its ini-

tial state. The manufacturer reports a preparation and application time of approximately 9 minutes at a room temperature of 20 °C for this cement. It was ensured that morphing was completed within the specified time frame for all experiments by applying the systematic approach depicted in Fig. 3b–c and Supplementary Video 1. Since we were working in a quasi-static manner where the dynamics was unimportant, the cement is not expected to have affected the outcome of the morph. When considering dynamics, one should consider that viscosity influences the rotation rate of the joints.

The mechanical testing method with a custom fixture was designed to test the relative strength of structures that are initially 2-D and deform to adapt to different 3-D curvatures. The same loading conditions

were applied to the different shapes to facilitate comparison. An out-of-plane compression test between two plates [43] does not ensure the same number of contact points between the structure and the plate. For example, a spherical surface has only one contact point with a flat plate, whereas a cylindrical surface has a contact line. This type of loading alters the conditions on a case-by-case basis, depending on the shape. The fixture used in this study aims to mitigate the consequences of this issue by distributing the load evenly across different shapes. The number of contact points remains equal for the same structure in different shapes, and the load is distributed in parallel across these contact points. The zigzagging of the low-friction wire ensures this load distribution. Once a fracture arises in the structure, the load conditions alter, and the measured load values lose significance.

4. Conclusions

This study investigated the kinematic deformation of additively manufactured chain mail-like structures made from a medical-grade titanium alloy regarding their shape-matching and locking capabilities. These structures, composed of rigid parts connected by ball-and-socket joints, could reinforce curved surfaces by forming a mesh and locking the joints once the desired shape was achieved.

A discrete multibody modeling approach was used to predict the kinematic behavior. Simulations identified three key parameters affecting shape conformity: the network pattern (*i.e.*, body shape), the ratio of body size to strut length, and the rotational orientation of the structure relative to the surface. Among the three patterns studied, triangular bodies provided the best shape-matching results, followed by square and hexagonal bodies. Increasing the strut-to-body size ratio improved shape conformity overall. At the same time, rotational orientation, *i.e.*, how the structure's pattern aligns with the shape's curvature pattern, only played a role for the square bodies.

Experiments were performed to validate the simulations. The designs were manufactured from medical grade Ti6Al4V ELI using PBF-LB. The specimens were placed in three generic shapes: saddle, cylinder, and spheroid. 3-D-scanning the configuration showed that the employed multibody model can predict the shape-matching qualities of the specimens. Subsequent mechanical tests showed the locking strength of the designs. In terms of shape-morphing quality, the tiling pattern ranks in ascending order from triangle to square to hexagon, with the triangle performing about two orders (10^2) better than square and four orders (10^4) better than hexagon in terms of fitting error. This behavior is the opposite in terms of mechanical performance, with a hexagon resisting an approximately two times higher load before fracture than a square and about three times higher load before fracture than a triangle.

CRediT authorship contribution statement

Pier H. de Jong: Writing – review & editing, Writing – original draft, Visualization, Validation, Software, Resources, Methodology, Investigation, Formal analysis, Data curation, Conceptualization. **Vahid Moosabeiki:** Writing – review & editing, Validation, Resources, Methodology, Investigation, Data curation, Conceptualization. **Marius A. Leeflang:** Writing – review & editing, Resources, Methodology, Investigation, Conceptualization. **Mohammad J. Mirzaali:** Writing – review & editing, Supervision, Methodology, Conceptualization. **Amir A. Zadpoor:** Writing – review & editing, Supervision, Project administration, Funding acquisition, Conceptualization.

Declaration of competing interest

The authors declare the following financial interests/personal relationships which may be considered as potential competing interests: Pier H. de Jong reports equipment, drugs, or supplies was provided by Heraeus Medical GmbH. If there are other authors, they declare that they have no known competing financial interests or personal relationships that could have appeared to influence the work reported in this paper.

Appendix A. Supplementary material

Supplementary material related to this article can be found online at https://doi.org/10.1016/j.matdes.2025.114471.

Data availability

Data will be made available upon request.

References

[1] E.T. Roche, et al., Soft robotic sleeve supports heart function, Sci. Transl. Med. 9 (2017) eaaf3925, https://www.science.org/doi/10.1126/scitranslmed.aaf3925.

[2] T.S. Lumpe, K. Shea, Computational design of multi-state lattice structures with finite mechanisms for shape morphing, J. Mech. Des. 145 (2023) 071701, https://asmedigitalcollection.asme.org/mechanicaldesign/article/145/7/071701/1159634/Computational-Design-of-Multi-State-Lattice.

[3] L. Ren, et al., Biology and bioinspiration of soft robotics: actuation, sensing, and system integration, iScience 24 (2021) 103075, https://linkinghub.elsevier.com/retrieve/pii/S2589004221010439.

[4] X. Yang, et al., Morphing matter: from mechanical principles to robotic applications, Soft Science, vol. 3, OAE Publishing Inc., 2023, https://www.oaepublish.com/articles/ss.2023.42.

[5] J. Sun, Q. Guan, Y. Liu, J. Leng, Morphing aircraft based on smart materials and structures: a state-of-the-art review, J. Intell. Mater. Syst. Struct. 27 (2016) 2289–2312, https://journals.sagepub.com/doi/10.1177/1045389X16629569.

[6] S. Daynes, P.M. Weaver, Review of shape-morphing automobile structures: concepts and outlook, Proc. Inst. Mech. Eng. Part D, J. Automob. Eng. 227 (2013) 1603–1622, http://journals.sagepub.com/doi/10.1177/0954407013496557.

[7] A. Riccio, A. Sellitto, M. Battaglia, Morphing spoiler for adaptive aerodynamics by shape memory alloys, Actuators 13 (2024) 330, https://www.mdpi.com/2076-0825/13/9/330.

[8] R.J. Morrison, et al., Mitigation of tracheobronchomalacia with 3D-printed personalized medical devices in pediatric patients, Sci. Transl. Med. 7 (2015), https://www.science.org/doi/10.1126/scitranslmed.3010825.

[9] J.M. Haglin, et al., Patient-specific orthopaedic implants, Orthop. Surg. 8 (2016) 417–424, https://onlinelibrary.wiley.com/doi/10.1111/os.12282.

[10] K.C. Wong, 3D-printed patient-specific applications in orthopedics, Orthop. Res. Rev. 8 (2016) 57–66, https://www.dovepress.com/3d-printed-patient-specific-applications-in-orthopedics-peer-reviewed-article-ORR.

[11] T.-y. Hsieh, R. Dedhia, B. Cervenka, T.T. Tollefson, 3D printing: current use in facial plastic and reconstructive surgery, Curr. Opin. Otolaryngol. Head Neck Surg. 25 (2017) 291–299, https://journals.lww.com/00020840-201708000-00008.

[12] I. Valverde, et al., Three-dimensional printed models for surgical planning of complex congenital heart defects: an international multicentre study, Eur. J. Cardio-Thorac. Surg. 52 (2017) 1139–1148, http://academic.oup.com/ejcts/article/52/6/1139/3925909.

[13] Y.J. Choo, M. Boudier-Revéret, M.C. Chang, 3D printing technology applied to orthosis manufacturing: narrative review, Ann. Palliat. Med. 9 (2020) 4262–4270, http://apm.amegroups.com/article/view/52460/html.

[14] N. Wallace, N.E. Schaffer, I.S. Aleem, R. Patel, 3D-printed patient-specific spine implants: a systematic review, Clin. Spine Surg. 33 (2020) 400–407, https://journals.lww.com/10.1097/BSD.0000000000001026.

[15] H. Aiba, et al., Current concepts in the resection of bone tumors using a patient-specific three-dimensional printed cutting guide, Curr. Oncol. 30 (2023) 3859–3870, https://www.mdpi.com/1718-7729/30/4/292.

[16] C. Benignus, et al., Patient specific instruments and patient individual implants—a narrative review, J. Pers. Med. 13 (2023) 426, https://www.mdpi.com/2075-4426/13/3/426.

[17] H.N. Singh, S. Agrawal, Y.K. Modi, Additively manufactured patient specific implants: a review, Arch. Mech. Eng. (2024), https://journals.pan.pl/dlibra/publication/149635/edition/130627/content.

[18] E.M. Zanetti, et al., Additive manufacturing of metal load-bearing implants 1: geometric accuracy and mechanical challenges, Chem. Ing. Tech. 96 (2024) 486–501, https://onlinelibrary.wiley.com/doi/10.1002/cite.202300171.

[19] E.M. Zanetti, et al., Additive manufacturing of metal load-bearing implants 2: surface modification and clinical challenges, Chem. Ing. Tech. 96 (2024) 502–512, https://onlinelibrary.wiley.com/doi/10.1002/cite.202300172.

[20] M. Oldhoff, M. Mirzaali, N. Tümer, J. Zhou, A. Zadpoor, Comparison in clinical performance of surgical guides for mandibular surgery and temporomandibular joint implants fabricated by additive manufacturing techniques, J. Mech. Behav. Biomed. Mater. 119 (2021) 104512, https://linkinghub.elsevier.com/retrieve/pii/S1751616121001971.

[21] A.M. DeHaan, J.R. Adams, M.L. DeHart, T.W. Huff, Patient-specific versus conventional instrumentation for total knee arthroplasty: peri-operative and cost differences, J. Arthroplast. 29 (2014) 2065–2069, https://linkinghub.elsevier.com/retrieve/pii/S0883540314004276.

[22] T. Small, et al., Comparison of acetabular shell position using patient specific instruments vs. Standard surgical instruments: a randomized clinical trial, J. Arthroplast. 29 (2014) 1030–1037, https://linkinghub.elsevier.com/retrieve/pii/S0883540313007882.

[23] I.M. Dorling, et al., Cost-effectiveness of patient specific vs conventional instrumentation for total knee arthroplasty: a systematic review and meta-analysis, World J. Orthop. 14 (2023) 458–470, https://www.wjgnet.com/2218-5836/full/v14/i6/458.htm.

[24] S. Ma, X. Zhang, S. Chen, The promises and challenges toward mass customization of healthcare services, Systems 12 (2024) 156, https://www.mdpi.com/2079-8954/12/5/156.

[25] P. Reimann, M. Brucker, D. Arbab, C. Lüring, Patient satisfaction - a comparison between patient-specific implants and conventional total knee arthroplasty, J. Orthop. 16 (2019) 273–277, https://linkinghub.elsevier.com/retrieve/pii/S0972978X19300364.

[26] D.H. Ballard, et al., Medical 3D printing cost-savings in orthopedic and maxillofacial surgery: cost analysis of operating room time saved with 3D printed anatomic models and surgical guides, Acad. Radiol. 27 (2020) 1103–1113, https://linkinghub.elsevier.com/retrieve/pii/S1076633219304180.

[27] P. Tack, J. Victor, P. Gemmel, L. Annemans, Do custom 3D-printed revision acetabular implants provide enough value to justify the additional costs? The health-economic comparison of a new porous 3D-printed hip implant for revision arthroplasty of Paprosky type 3B acetabular defects and its closest alternative, Orthop. Traumatol., Surg. Res. 107 (2021) 102600, https://linkinghub.elsevier.com/retrieve/pii/S1877056820301249.

[28] M. Lawless, et al., Review of cost and surgical time implications using virtual patient specific planning and patient specific implants in midface reconstruction, Plast. Aesthet. Res. 9 (2022) 26, https://www.oaepublish.com/articles/2347-9264.2021.108.

[29] M. Meng, et al., 3D printing metal implants in orthopedic surgery: methods, applications and future prospects, J. Orthop. Transl. 42 (2023) 94–112, https://linkinghub.elsevier.com/retrieve/pii/S2214031X2300058X.

[30] S. Attarilar, et al., 3D printing technologies in metallic implants: a thematic review on the techniques and procedures, Int. J. Bioprint. 7 (2024) 306, https://accscience.com/journal/IJB/7/1/10.18063/ijb.v7i1.306.

[31] S. Leeflang, S. Janbaz, A.A. Zadpoor, Metallic clay, Addit. Manuf. 28 (2019) 528–534, https://linkinghub.elsevier.com/retrieve/pii/S2214860419302027.

[32] P.H. de Jong, A.L. Schwab, M.J. Mirzaali, A.A. Zadpoor, A multibody kinematic system approach for the design of shape-morphing mechanism-based metamaterials, Commun. Mater. 4 (2023) 83, https://www.nature.com/articles/s43246-023-00410-2.

[33] P.H. de Jong, Y. Salvatori, F. Libonati, M.J. Mirzaali, A.A. Zadpoor, Shape-locking in architected materials through 3D printed magnetically activated joints, Mater. Des. 235 (2023) 112427, https://www.sciencedirect.com/science/article/pii/S0264127523008420.

[34] E. García-Rey, R. Madero, E. García-Cimbrelo, THA Revisions Using Impaction Allografting with Mesh Is Durable for Medial but Not Lateral Acetabular Defects, Clinical Orthopaedics & Related Research, vol. 473, Ovid Technologies (Wolters Kluwer Health), 2015, pp. 3882–3891, https://journals.lww.com/00003086-201512000-00034.

[35] V. Moosabeiki, et al., Additively manufactured shape-morphing implants for the treatment of acetabular defects, Acta Biomater. (2025), https://linkinghub.elsevier.com/retrieve/pii/S1742706125005112.

[36] J. Wang, A. Chortos, Performance metrics for shape-morphing devices, Nat. Rev., Mater. 9 (2024) 738–751, https://www.nature.com/articles/s41578-024-00714-w.

[37] M.M. Yuan, B.H. Sun, Adjustable stiffness of chain mail fabrics, Compos. Struct. 368 (2025) 119237, https://linkinghub.elsevier.com/retrieve/pii/S0263822325004027.

[38] S.J. Callens, A.A. Zadpoor, From flat sheets to curved geometries: origami and kirigami approaches, Mater. Today 21 (2018) 241–264, https://linkinghub.elsevier.com/retrieve/pii/S1369702117306399.

[39] S.J. Callens, N. Tümer, A.A. Zadpoor, Hyperbolic origami-inspired folding of triply periodic minimal surface structures, Appl. Mater. Today 15 (2019) 453–461, https://linkinghub.elsevier.com/retrieve/pii/S2352940719300824.

[40] S.J.P. Callens, et al., Emergent collective organization of bone cells in complex curvature fields, Nat. Commun. 14 (2023) 855, https://www.nature.com/articles/s41467-023-36436-w.

[41] B. Grünbaum, G.C. Shephard, Tilings by regular polygons, Math. Mag. 50 (1977) 227–247, https://www.tandfonline.com/doi/full/10.1080/0025570X.1977.11976655.

[42] D. Chavey, Tilings by regular polygons - II a catalog of tilings, in: Symmetry 2, Elsevier, 1989, pp. 147–165, https://linkinghub.elsevier.com/retrieve/pii/B9780080372372500192.

[43] L. Dreier, T.J. Jones, A. Plummer, A. Košmrlj, P.-T. Brun, Beaded metamaterials, http://arxiv.org/abs/2404.04227, arXiv:2404.04227 [cond-mat], 2024.

[44] S. Krivoshapko, V. Ivanov, Encyclopedia of Analytical Surfaces, Springer International Publishing, Cham, 2015, http://link.springer.com/10.1007/978-3-319-11773-7.

[45] F. Minding, Wie sich entscheiden läfst, ob zwei gegebene krumme Flächen auf einander abwickelbar sind oder nicht; nebst Bemerkungen über die Flächen von unveränderlichem Krümmungsmaafse, vol. 19, De Gruyter, 1839, pp. 370–387, https://www.degruyter.com/document/doi/10.1515/9783112389867-019/html.

[46] P. Carretero, I. Castro, A new approach to rotational Weingarten surfaces, Mathematics 10 (2022) 578, https://www.mdpi.com/2227-7390/10/4/578.

[47] M. Hadzhilazova, I.M. Mladenov, J. Oprea, Unduloids and their geometry, Arch. Math. 43 (2007) 417–429, http://dml.cz/dmlcz/108081.

[48] M. Leeflang, F. Bobbert, A. Zadpoor, Additive manufacturing of non-assembly deployable mechanisms for the treatment of large bony defects, Addit. Manuf. 46 (2021) 102194, https://linkinghub.elsevier.com/retrieve/pii/S2214860421003560.

[49] ISO & ASTM, 52900 Additive manufacturing - General principles - Fundamentals and vocabulary, 2021.

[50] F. Crameri, G.E. Shephard, P.J. Heron, The misuse of colour in science communication, Nat. Commun. 11 (2020) 5444, https://www.nature.com/articles/s41467-020-19160-7.